Int. J. Appl. Math. Comput. Sci., 2020, Vol. 30, No. 1, 113–122
DOI: 10.34768/amcs-2020-0009

A SECOND–ORDER TV–BASED COUPLING MODEL AND AN ADMM ALGORITHM FOR MR IMAGE RECONSTRUCTION

BO ZHOU [a,b,*], YU-FEI YANG [c,a], BO-XIA HU [a,d]

[a]College of Mathematics and Econometrics
Hunan University
Changsha 410082, Hunan, China
e-mail: 64553433@qq.com

[b]College of Computer Science and Electronic Engineering
Hunan University
Changsha 410082, Hunan, China

[c]School of Computer Engineering and Applied Mathematics
Changsha University
Changsha 410003, Hunan, China
e-mail:yangyufei_hd@sina.com

[d]College of Mathematics and Statistics
Hengyang Normal University
Hengyang 421000, Hunan, China

Motivated by ideas from two-step models and combining second-order TV regularization in the LLT model, we propose a coupling model for MR image reconstruction. By applying the variables splitting technique, the split Bregman iterative scheme, and the alternating minimization method twice, we can divide the proposed model into several subproblems only related to second-order PDEs so as to avoid solving a fourth-order PDE. The solution of every subproblem is based on generalized shrinkage formulas, the shrink operator or the diagonalization technique of the Fourier transform, and hence can be obtained very easily. By means of the Barzilai–Borwein step size selection scheme, an ADMM type algorithm is proposed to solve the equations underlying the proposed model. The results of numerical implementation demonstrate the feasibility and effectiveness of the proposed model and algorithm.

Keywords: MRI reconstruction, LLT model, LOT model, coupling model, ADMM, split Bregman, wavelet transform.

1. Introduction

Magnetic resonance (MR) imaging is a non-invasive and non-ionizing imaging technique which enables excellent visualization of both anatomical structures and physiological functions. However, this imaging modality is time-consuming because data samples in MR imaging are acquired sequentially in k-space (Yang *et al*., 2010; Miao *et al*., 2011) of the spatial Fourier transform of the object. Therefore, many MR techniques (Yang *et al*., 2010; Miao *et al*., 2011), including compressive sensing (CS) (Lustig *et al*., 2007), have been developed to reduce the amount of data needed for accurate reconstruction.

There are many PDE-based models to solve the MR image reconstruction problem, e.g., the TVL$_1$-L$_2$ model introduced by Yang *et al*. (2010). Based on total variation (TV) regularization and wavelets, Lustig *et al*. (2007) proposed a constrained minimization model as follows:

$$\min_u \|u\|_{TV} + \alpha\|\Phi^\top u\|_1,$$

subject to

$$\|Au - f\|_2 < \sigma, \tag{1}$$

*Corresponding author

where

$$\|u\|_{TV} = \|\nabla u\|_1 = \int_\Omega |\nabla u| \, \mathrm{d}x,$$
$$|\nabla u| = \sqrt{(\nabla_x u)^2 + (\nabla_y u)^2},$$

u represents the reconstructed image and Φ is the wavelet transform, $\|\cdot\|_1$ is the L_1 norm and the superscript $^\top$ is the conjugate transpose of a matrix, A is the partial Fourier operator, f denotes partially scanned k space data and σ is an estimate of the noise level in the data. TV regularization and wavelet transforms can be regarded as forcing the MR image to be sparse.

Several fast algorithms (Chen *et al*., 2012; Yang *et al*., 2010; Ye *et al*., 2011) have been developed to solve the unconstrained version of the model (1) (called the TVL_1 model):

$$\min_u \|u\|_{TV} + \alpha\|\Phi^\top u\|_1 + \frac{\beta}{2}\|Au - f\|_2^2, \qquad (2)$$

where β is a regularization parameter. These algorithms involved only the computation of shrinkage operators and the fast Fourier transform. Especially, the Barzilai–Borwein (BB) step size selection scheme was adopted by Ye *et al*. (2011) for faster convergence, and only an explicit system needs to be solved because the efficiency of the proposed algorithm did not rely on the fact that A^TA could be diagonalized by fast transforms.

The second order model of PDE-based image reconstruction like (1) has a TV-based regularization term, which was introduced by Rudin *et al*. (1992) for image denoising (called the ROF model). Unfortunately, TV regularization suffers from the so-called staircase effect, i.e., the convertion of smooth regions into piecewise constant ones, which may generate block-like images. In order to overcome the inherent shortcoming of TV regularization, some higher order models have been developed (Lysaker *et al*., 2003; Steidl, 2006; You and Kaveh, 2000), such as the LLT model proposed by Lysaker *et al*. (2003), the corresponding numerical methods are also similar to those of the ROF model. Inspired by the LLT model, Xie *et al*. (2014) proposed a higher-order model for MR image reconstruction in the following (called the $\mathrm{TV}^2\mathrm{L}_1$ model):

$$\min_u \|u\|_{TV^2} + \alpha\|\Phi^\top u\|_1 + \frac{\beta}{2}\|Au - f\|_2^2, \qquad (3)$$

where

$$\|u\|_{TV^2} = \|\nabla^2 u\|_1 = \int_\Omega |\nabla^2 u| \, \mathrm{d}x,$$
$$\nabla^2 u = \begin{bmatrix} \nabla_{xx} u & \nabla_{xy} u \\ \nabla_{yx} u & \nabla_{yy} u \end{bmatrix},$$
$$|\nabla^2 u| = \sqrt{(\nabla_{xx} u)^2 + (\nabla_{xy} u)^2 + (\nabla_{yx} u)^2 + (\nabla_{yy} u)^2}.$$

However, it is more difficult to solve higher-order models than the ROF one since some high-order derivatives are included in these models. In addition, they tend to introduce some blurring in regions of image edges.

In order to avoid the staircase effect while alleviating edge blurring, Lysaker *et al*. (2004) proposed a two-step method for image denoising (called the LOT model). The first step of the classic LOT model (Lysaker *et al*., 2004) is to solve the following problem:

$$\min_{|\boldsymbol{n}|=1} \int_\Omega |\nabla \boldsymbol{n}| \, \mathrm{d}x + \frac{\alpha}{2} \int_\Omega \Big(\boldsymbol{n} - \frac{\nabla f}{|\nabla f|}\Big)^2 \mathrm{d}x, \qquad (4)$$

where the first term is the regularization term, $|\nabla \boldsymbol{n}|$ is the total variation of the unit normal vector $\boldsymbol{n}$ for the level curves of image u, and α is a regularization parameter. The second step is to reconstruct the restored image u by solving the following minimization problem:

$$\min_u \int_\Omega (|\nabla u| - \boldsymbol{n}^* \cdot \nabla u) \, \mathrm{d}x + \frac{\beta}{2} \int_\Omega (u - f)^2 \, \mathrm{d}x, \qquad (5)$$

where $\boldsymbol{n}^*$ is the solution of (4) and β is a regularization parameter. The LOT model may restore edges and discontinuities in a better way than the LLT one while alleviating the staircase effect. However, if the information about the noise is not known, the LOT model cannot preserve edges or textures well. Furthermore, three discrete nonlinear second-order PDEs derived from the LOT model have to be computed so that algorithms for solving model equations are slow.

For the sake of overcoming the drawbacks of the above models, motivated by the ideas from two-step models (Dong *et al*., 2009; Hao *et al*., 2012; Yang *et al*., 2011) and by combining second-order TV regularization in the LLT model (Lysaker *et al*., 2003), in this paper, we propose a novel model coupling two variables for MR image reconstruction. By using the variables splitting technique, the split Bregman iterative scheme, and the alternating minimization method (Chan *et al*., 2011), we can divide the proposed model into five subproblems. In order to avoid solving a fourth-order PDE, we use again the variables splitting technique and the split Bregman iterative scheme so that in this paper we only need to solve second-order PDEs with less computation based on generalized shrinkage formulas, the shrink operator and the diagonalization technique of the Fourier transform. The Barzilai–Borwein step size selection scheme (Wright *et al*., 2009) is also adopted to accelerate convergence. On this basis, we propose an ADMM-type algorithm to solve the proposed model. Several numerical experiments are carried out, and the experimental results indicate that the proposed algorithm is efficient and can provide better MR reconstructed images.

The organization of this paper is as follows. In the next section, we first propose a second-order TV-based

coupling model for MR image reconstruction. Then, by applying the split Bregman iterative scheme twice and based on generalized shrinkage formulas, the shrink operator, and the diagonalization technique of the Fourier transform, we propose an ADMM type algorithm to solve the proposed model. Some numerical experiments are implemented in Section 3 to verify the feasibility and effectiveness of the proposed model and algorithm. In the last section, we provide some concluding remarks.

Some symbols are introduced in this paper: $u \in \mathbb{R}^N$ is the objective image consisting of N pixels. $\Phi^\top = (\phi_1, \phi_2, \ldots, \phi_n)^\top \in \mathbb{C}^{N\times N}$ is usually a proper orthogonal matrix (e.g., the Haar wavelet) sparsifying the underlying image u, $f \in \mathbb{C}^M$ with $M \leq N$ is the partially scanned data and $R \in \mathbb{R}^{M\times N}$ is the binary matrix representing the sampling pattern. Noting that the Fourier transform $\mathcal{F}$ is in fact an $N \times N$ unitary matrix, $A = R\mathcal{F}$ is the partial Fourier transform operator.

2. Coupling model and the ADMM algorithm

Inspired by the advantages in the classical LOT model (Lysaker *et al*., 2004), a deformation of the LOT model has been developed (Dong *et al*., 2009; Hao *et al*., 2012; Yang *et al*., 2011). In the first step, instead of smoothing the unit normal vector $\boldsymbol{n}$ as in the LOT model (Lysaker *et al*., 2004), the authors smoothed the angle θ, where $\boldsymbol{n} = (\cos\theta, \sin\theta)$, thus only one variable was solved so as to speed the computation. The two models proposed in the two-step method (Yang *et al*., 2011) are as follows:

$$\begin{cases} \min\limits_{\theta} \int_\Omega |\nabla\theta|\,\mathrm{d}x + \frac{\alpha}{2}\int_\Omega (\theta-\theta_0)^2\,\mathrm{d}x, \\ \min\limits_{u} \int_\Omega (|\nabla u| - (\cos\theta,\sin\theta)\cdot\nabla u)\,\mathrm{d}x \\ \qquad +\frac{\beta}{2}\int_\Omega (u-f)^2\,\mathrm{d}x, \end{cases} \tag{6}$$

where $\theta_0 = \operatorname{atan}(u_{0y}/u_{0x})$, $(u_{0x}, u_{0y})^\top = \nabla f/|\nabla f|$.

Motivated by the above ideas and by combining second-order TV regularization in the LLT model (Lysaker *et al*., 2003), in this paper, we propose a novel model coupling two variables θ and u for MR image reconstruction (2) expressed as follows:

$$\begin{aligned} \min_{\theta,u} &\int_\Omega |\nabla\theta|\,\mathrm{d}x + \lambda\int_\Omega |\Phi^\top u|_1\,\mathrm{d}x + \lambda_1\int_\Omega |\nabla^2 u|\,\mathrm{d}x \\ &+ \frac{\alpha}{2}\int_\Omega (\theta-\theta_0)^2\,\mathrm{d}x + \frac{\beta}{2}\int_\Omega (Au-f)^2\,\mathrm{d}x \\ &+ \frac{\gamma}{2}\int_\Omega (|\nabla u| - (\cos\theta,\sin\theta)\cdot\nabla u)^2\,\mathrm{d}x. \end{aligned} \tag{7}$$

In order to avoid numerical difficulties caused by nonsmooth terms in (7), we apply the split Bregman iterative scheme to solve the above model. Firstly, we introduce an auxiliary variable $\boldsymbol{\eta}$ to transform $\nabla\theta$ with $\boldsymbol{\eta} = (\eta_1, \eta_2)^\top = (\nabla_x\theta, \nabla_y\theta)^\top$. Secondly, we use an auxiliary variable z to transform $\Phi^\top u$. Thirdly, we introduce auxiliary variable v to transform ∇u with $\boldsymbol{v} = \nabla u = (\nabla_x u, \nabla_y u)^\top$. Then we can turn (7) into the following constrained optimization problem:

$$\begin{aligned} \min_{u,\theta,\boldsymbol{\eta},z,\boldsymbol{v}} &\int_\Omega |\boldsymbol{\eta}|\,\mathrm{d}x + \lambda\int_\Omega |z|_1\,\mathrm{d}x + \lambda_1\int_\Omega |\nabla\boldsymbol{v}|\,\mathrm{d}x \\ &+ \frac{\alpha}{2}\int_\Omega (\theta-\theta_0)^2\,\mathrm{d}x + \frac{\beta}{2}\int_\Omega (Au-f)^2\,\mathrm{d}x \\ &+ \frac{\gamma}{2}\int_\Omega (|\boldsymbol{v}| - (\cos\theta,\sin\theta)\cdot\boldsymbol{v})^2\,\mathrm{d}x, \end{aligned} \tag{8}$$

subject to

$$\boldsymbol{\eta} = \nabla\theta, \quad z = \Phi^\top u, \quad \boldsymbol{v} = \nabla u,$$

where

$$\nabla\boldsymbol{v} = \begin{bmatrix} \nabla_x v_1 & \nabla_y v_1 \\ \nabla_x v_2 & \nabla_y v_2 \end{bmatrix},$$

$$|\nabla\boldsymbol{v}| = \sqrt{(\nabla_x v_1)^2 + (\nabla_y v_1)^2 + (\nabla_x v_2)^2 + (\nabla_y v_2)^2}.$$

The related augmented Lagrangian functional can be written as

$$\begin{aligned} &L(u,\theta,\boldsymbol{\eta},z,\boldsymbol{v};\boldsymbol{a},b,\boldsymbol{c}) \\ &= \|\boldsymbol{\eta}\| + \frac{\rho_1}{2}\|\eta_1 - \nabla_x\theta - a_1\|_2^2 + \frac{\rho_1}{2}\|\eta_2 - \nabla_y\theta - a_2\|_2^2 \\ &\quad + \lambda\left(\|z\|_1 + \frac{\rho_2}{2}\|z - \Phi^\top u - b\|_2^2\right) + \lambda_1\|\nabla\boldsymbol{v}\| \\ &\quad + \lambda_1\left(\frac{\rho_3}{2}\|v_1 - \nabla_x u - c_1\|_2^2 + \frac{\rho_3}{2}\|v_2 - \nabla_y u - c_2\|_2^2\right) \\ &\quad + \frac{\alpha}{2}\|\theta-\theta_0\|_2^2 + \frac{\beta}{2}\|Au-f\|_2^2 \\ &\quad + \frac{\gamma}{2}\||\boldsymbol{v}| - (\cos\theta,\sin\theta)\cdot\boldsymbol{v}\|_2^2, \end{aligned} \tag{9}$$

where $\boldsymbol{a} = (a_1, a_2)^\top \in \mathbb{C}^{N\times 2N}$, $b \in \mathbb{C}^N$ and $\boldsymbol{c} = (c_1, c_2)^\top \in \mathbb{C}^{2N}$ are the Lagrangian multipliers, while ρ_1, ρ_2 and ρ_3 are positive penalty parameters.

By applying the Bregman iteration to (8), we get the following iteration scheme with minimizing L in (9) with respect to $(u, \theta, \boldsymbol{\eta}, z, \boldsymbol{v})$ and with the updates of the multipliers $\boldsymbol{a}$, b and $\boldsymbol{c}$:

$$\begin{cases} (u^{k+1}, \theta^{k+1}, \boldsymbol{\eta}^{k+1}, z^{k+1}, \boldsymbol{v}^{k+1}) = \\ \qquad \arg\min\limits_{u,\theta,\boldsymbol{\eta},z,\boldsymbol{v}} L(u,\theta,\boldsymbol{\eta},z,\boldsymbol{v};\boldsymbol{a}^k,b^k,\boldsymbol{c}^k), \\ a_1^{k+1} = a_1^k + \kappa_1(\nabla_x\theta^{k+1} - \eta_1^{k+1}), \\ a_2^{k+1} = a_2^k + \kappa_1(\nabla_y\theta^{k+1} - \eta_2^{k+1}), \\ b^{k+1} = b^k + \kappa_2(\Phi^\top u^{k+1} - z^{k+1}), \\ c_1^{k+1} = c_1^k + \kappa_3(\nabla_x u^{k+1} - v_1^{k+1}), \\ c_2^{k+1} = c_2^k + \kappa_3(\nabla_y u^{k+1} - v_2^{k+1}). \end{cases} \tag{10}$$

Based on the alternating minimization method (Chan *et al*., 2011), we can divide the minimization problem in

(10) into the following five subproblems:

$$u^{k+1} = \arg\min_{u} \lambda\rho_2\|z^k - \Phi^\top u - b^k\|_2^2 + \beta\|Au - f\|_2^2 + \lambda_1\rho_3\|\boldsymbol{v}^k - \nabla u - \boldsymbol{c}^k\|_2^2, \quad (11)$$

$$\theta^{k+1} = \arg\min_{\theta} \rho_1\|\boldsymbol{\eta}^k - \nabla\theta - \boldsymbol{a}^k\|_2^2 + \alpha\|\theta - \theta_0\|_2^2 + \gamma\||\boldsymbol{v}^k| - (\cos\theta, \sin\theta)\cdot\boldsymbol{v}^k\|_2^2, \quad (12)$$

$$(\eta_1^{k+1}, \eta_2^{k+1}) = \arg\min_{\eta_1,\eta_2} \|\boldsymbol{\eta}\| + \frac{\rho_1}{2}\|\boldsymbol{\eta} - \nabla\theta^{k+1} - \boldsymbol{a}^k\|_2^2, \quad (13)$$

$$z^{k+1} = \arg\min_{z} \|z\|_1 + \frac{\rho_2}{2}\|z - \Phi^\top u^{k+1} - b^k\|_2^2, \quad (14)$$

$$\boldsymbol{v}^{k+1} = \arg\min_{v} 2\lambda_1\|\nabla\boldsymbol{v}\| + \lambda_1\rho_3\|\boldsymbol{v} - \nabla u^{k+1} - \boldsymbol{c}^k\|_2^2 + \gamma\||\boldsymbol{v}| - (\cos\theta^{k+1}, \sin\theta^{k+1})\cdot\boldsymbol{v}\|_2^2. \quad (15)$$

It is obvious that updating the multipliers such as a_1^k, a_2^k ,b^k, c_1^k and c_2^k is easy. How to efficiently solve each of the subproblems (11) to (15) will be discussed in the forthcoming subsections.

2.1. u-Subproblem. In this subsection, we discuss how to solve the u-subproblem (11). The problem (11) cannot be solved directly using the fast Fourier transform, as pointed out by Ye *et al.* (2011), if $A^\top A$ cannot be diagonalized. Otherwise, the efficiency of the fast algorithm would be lost. To overcome this shortcoming, as done by Xie *et al.* (2014), quadratic approximation of the function $H(u) = \frac{1}{2}\|Au - f\|_2^2$ at point u^k,

$$Q_\delta(u, u^k) = H(u^k) + \langle\nabla H(u^k), u - u^k\rangle + \frac{\delta}{2}\|u - u^k\|_2^2,$$

can be used to replace $H(u)$ in (11); it is actually a linearization of $H(u)$ at point u^k plus a proximity term penalized by parameter $\delta > 0$. On account of $\nabla H(u) = A^\top(Au - f)$, adopting the Barzilai–Borwein step size selection scheme (Wright *et al.*, 2009) to update the step size δ as done by Xie *et al.* (2014) or Ye *et al.* (2011) for accelerating convergence, we can transform the minimization subproblem (11) into the following form:

$$u^{k+1} = \arg\min_{u} \lambda\rho_2\|z^k - \Phi^\top u - b\|_2^2 + 2\beta Q_\delta(u, u^k) + \lambda_1\rho_3\|\boldsymbol{v}^k - \nabla u - \boldsymbol{c}^k\|_2^2,$$

i.e.,

$$u^{k+1} = \arg\min_{u} \lambda\rho_2\|z^k - \Phi^\top u - b\|_2^2 + \beta\delta_k\|u - u^k + \delta_k^{-1}A^\top(Au^k - f)\|_2^2 + \lambda_1\rho_3\|\boldsymbol{v}^k - \nabla u - \boldsymbol{c}^k\|_2^2. \quad (16)$$

On the basis of the necessary optimality condition, in view of $\Delta = -(\nabla_x^\top\nabla_x + \nabla_y^\top\nabla_y)$ and $\Phi\Phi^\top = I$, we can deduce the solution of the u-subproblem (16), given by the solution of the equation

$$L_1^k u^{k+1} = \mathrm{RHS}_1^k, \quad (17)$$

where

$$L_1^k = \lambda\rho_2 I + \beta\delta_k I - \lambda_1\rho_3\Delta,$$
$$\mathrm{RHS}_1^k = \lambda_1\rho_3\nabla_x^\top(v_1^k - c_1^k) + \lambda_1\rho_3\nabla_y^\top(v_2^k - c_2^k) + \lambda\rho_2\Phi(z^k - b^k) + \beta\delta_k u^k - \beta A^\top(Au^k - f).$$

Since the Laplace operator is block circular under the periodic boundary condition and can be diagonalized by Fourier transform $\mathcal{F}$ with the property $\mathcal{F}^\top = \mathcal{F}^{-1}$, Eqn. (17) can be converted to

$$\mathcal{F}^\top\hat{L}_1^k\mathcal{F}u^{k+1} = \mathrm{RHS}_1^k, \quad (18)$$

where $\hat{L}_1^k = \lambda\rho_2 I + \beta\delta_k I - \lambda_1\rho_3\mathcal{F}\Delta\mathcal{F}^\top$. Since $\hat{L}_1^k$ is diagonal, the above equation can be solved easily.

By making use of the Barzilai–Borwein (BB) step size selection scheme proposed by Wright *et al.* (2009), the iterative step size δ_{k+1} can be computed by solving

$$\arg\min_{\delta} \|\nabla H(u^{k+1}) - \nabla H(u^k) - \delta(u^{k+1} - u^k)\|_2^2,$$

which also implies

$$\delta_{k+1} = \frac{\langle\nabla H(u^{k+1}) - \nabla H(u^k), u^{k+1} - u^k\rangle}{\|u^{k+1} - u^k\|_2^2} = \frac{\|A(u^{k+1} - u^k)\|_2^2}{\|u^{k+1} - u^k\|_2^2}. \quad (19)$$

2.2. θ-Subproblem. To speed up the efficiency of solving the θ-subproblem (12), we replace the variable θ_0 in (12) with θ^k so that the θ-subproblem is transformed into the following one:

$$\theta^{k+1} = \arg\min_{\theta} \rho_1\|\eta_1^k - \nabla_x\theta - a_1^k\|_2^2 + \rho_1\|\eta_2^k - \nabla_y\theta - a_2^k\|_2^2 + \alpha\|\theta - \theta^k\|_2^2 + \gamma\||\boldsymbol{v}^k| - (\cos\theta, \sin\theta)\cdot\boldsymbol{v}^k\|_2^2. \quad (20)$$

Based on the optimality condition about θ, the above problem (20) can be solved by the following system:

$$(\alpha I - \rho_1\Delta)\theta = \gamma\left((-\sin\theta, \cos\theta)\cdot\boldsymbol{v}^k\right)\left(|\boldsymbol{v}^k| - (\cos\theta, \sin\theta)\cdot\boldsymbol{v}^k\right) + \alpha\theta^k + \rho_1\nabla_x^\top(\eta_1^k - a_1^k) + \rho_1\nabla_y^\top(\eta_2^k - a_2^k). \quad (21)$$

Solving Eqn. (21) directly is difficult, because there exist $\theta, \sin\theta, \cos\theta$ in (21) at the same time. To overcome this drawback, we replace $\sin\theta$, $\cos\theta$ in (21) with $\sin\theta^k$, $\cos\theta^k$, respectively, so that Eqn. (21) can be converted to the following simplified form:

$$\mathcal{F}^\top\hat{L}_2^k\mathcal{F}\theta^{k+1} = \mathrm{RHS}_2^k, \quad (22)$$

where $\hat{L}_2^k = \alpha I - \rho_1 \mathcal{F}\Delta\mathcal{F}^\top$,

$$\text{RHS} = \gamma\left((-\sin\theta^k, \cos\theta^k)\cdot \boldsymbol{v}^k\right),$$

$$\begin{aligned}\text{RHS}_2^k =& \text{RHS}\left(|\boldsymbol{v^k}| - (\cos\theta^k, \sin\theta^k)\cdot \boldsymbol{v}^k\right) + \alpha\theta^k \\ &+ \rho_1\nabla_x^\top(\eta_1^k - a_1^k) + \rho_1\nabla_y^\top(\eta_2^k - a_2^k).\end{aligned}$$

The use of the diagonalization technique of the Fourier transform makes the solution of Eqn. (22) very simple.

2.3. $\boldsymbol{\eta}, z$ Shrink-subproblem. By means of a generalized shrinkage formula, as done by Wang *et al.* (2007), the solution to the $\boldsymbol{\eta}$-subproblem (13) can be deduced as follows:

$$\begin{cases} \eta_1^{k+1} = \max\left(t_{k+1} - \frac{1}{\rho_1}, 0\right)\cdot \dfrac{\nabla_x\theta^{k+1} + a_1^k}{t_{k+1}}, \\ \eta_2^{k+1} = \max\left(t_{k+1} - \frac{1}{\rho_1}, 0\right)\cdot \dfrac{\nabla_y\theta^{k+1} + a_2^k}{t_{k+1}}, \end{cases} \tag{23}$$

where

$$t_{k+1} = \sqrt{(\nabla_x\theta^{k+1} + a_1^k)^2 + (\nabla_y\theta^{k+1} + a_2^k)^2}.$$

Based on the shrink operator, defined by

$$\text{shrink}(a, b) = \frac{a}{|a|}\max(a - \frac{1}{b}, 0),$$

we can deduce easily the solution of the z-subproblem (14) as follows:

$$z^{k+1} = \text{shrink}(\Phi^\top u^{k+1} + b^k, \frac{1}{\rho_2}). \tag{24}$$

2.4. $\boldsymbol{v}$-Subproblem. In this subsection, we discuss the solution of the $\boldsymbol{v}$-subproblem (15). As done by (Xie *et al.*, 2014), for the second time, we apply the split Bregman iterative scheme to solve the problem (15). By introducing the variable p subject to $p = \nabla\boldsymbol{v}$ and applying the augmented Lagrangian method, we can turn the minimization problem (15) into the following one:

$$\begin{cases} (\boldsymbol{v}^{k+1}, p^{k+1}) = \arg\min\limits_{\boldsymbol{v},p} 2\lambda_1\|p\| \\ \qquad +\lambda_1\rho_3\|\boldsymbol{v} - \nabla u^{k+1} - \boldsymbol{c}^k\|_2^2 \\ \qquad +\gamma\||\boldsymbol{v}| - (\cos\theta^{k+1}, \sin\theta^{k+1})\cdot\boldsymbol{v}\|_2^2 \\ \qquad +\lambda_1\rho_4\|p - \nabla\boldsymbol{v} - d^k\|_2^2, \\ d_{11}^{k+1} = d_{11}^k + \kappa_4(\nabla_x v_1^{k+1} - p_{11}^{k+1}), \\ d_{12}^{k+1} = d_{12}^k + \kappa_4(\nabla_y v_1^{k+1} - p_{12}^{k+1}), \\ d_{21}^{k+1} = d_{21}^k + \kappa_4(\nabla_x v_2^{k+1} - p_{21}^{k+1}), \\ d_{22}^{k+1} = d_{22}^k + \kappa_4(\nabla_y v_2^{k+1} - p_{22}^{k+1}), \end{cases} \tag{25}$$

where the variable d is the Lagrangian multiplier,

$$d = \begin{bmatrix} d_{11} & d_{12} \\ d_{21} & d_{22} \end{bmatrix}, \quad p = \begin{bmatrix} p_{11} & p_{12} \\ p_{21} & p_{22} \end{bmatrix},$$
$$|p| = \sqrt{p_{11}^2 + p_{12}^2 + p_{21}^2 + p_{22}^2}.$$

Based on the alternating minimization scheme (Chan *et al.*, 2011) and using a simplified computation for $\boldsymbol{v}^{k+1}$, the minimization problem in (25) can be turned into the following subproblems:

$$\begin{aligned} v_1^{k+1} =& \arg\min_{v_1} \lambda_1\rho_3\|v_1 - \nabla_x u^{k+1} - c_1^k\|_2^2 \\ &+ \gamma g_{k+1}\|v_1\|_2^2 + \lambda_1\rho_4\|p_{11}^k - \nabla_x v_1 - d_{11}^k\|_2^2 \\ &+ \lambda_1\rho_4\|p_{12}^k - \nabla_y v_1 - d_{12}^k\|_2^2, \end{aligned} \tag{26}$$

$$\begin{aligned} v_2^{k+1} =& \arg\min_{v_2} \lambda_1\rho_3\|v_2 - \nabla_y u^{k+1} - c_2^k\|_2^2 \\ &+ \gamma g_{k+1}\|v_2\|_2^2 + \lambda_1\rho_4\|p_{21}^k - \nabla_x v_2 - d_{21}^k\|_2^2 \\ &+ \lambda_1\rho_4\|p_{22}^k - \nabla_y v_2 - d_{22}^k\|_2^2, \end{aligned} \tag{27}$$

$$\begin{aligned} p_{11}^{k+1} =& \arg\min_{p_{11}} \|p\| \\ &+ \frac{\rho_4}{2}\|p_{11} - \nabla_x v_1^{k+1} - d_{11}^k\|_2^2, \end{aligned} \tag{28}$$

$$\begin{aligned} p_{12}^{k+1} =& \arg\min_{p_{12}} \|p\| \\ &+ \frac{\rho_4}{2}\|p_{12} - \nabla_y v_1^{k+1} - d_{12}^k\|_2^2, \end{aligned} \tag{29}$$

$$\begin{aligned} p_{21}^{k+1} =& \arg\min_{p_{21}} \|p\| \\ &+ \frac{\rho_4}{2}\|p_{21} - \nabla_x v_1^{k+1} - d_{21}^k\|_2^2, \end{aligned} \tag{30}$$

$$\begin{aligned} p_{22}^{k+1} =& \arg\min_{p_{12}} \|p\| \\ &+ \frac{\rho_4}{2}\|p_{22} - \nabla_y v_1^{k+1} - d_{22}^k\|_2^2, \end{aligned} \tag{31}$$

where

$$g_{k+1} = \left(1 - (\cos\theta^{k+1}, \sin\theta^{k+1})\cdot\frac{\nabla u^{k+1}}{|\nabla u^{k+1}|}\right)^2.$$

The v_1 subproblem (26) can be solved using its necessary optimality condition, given in the following system:

$$L_3^k v_1^{k+1} = \text{RHS}_3^k, \tag{32}$$

where

$$\begin{aligned} L_3^k &= \lambda_1\rho_3 I + \gamma g_{k+1} I - \lambda_1\rho_4\Delta, \\ \text{RHS}_3^k &= \lambda_1\rho_3(\nabla_x u^{k+1} + c_1^k) + \lambda_1\rho_4\nabla_x^\top(p_{11}^k - d_{11}^k) \\ &\quad + \lambda_1\rho_4\nabla_y^\top(p_{12}^k - d_{12}^k). \end{aligned}$$

Similarly, the v_2 subproblem (27) can be solved using the system

$$L_3^k v_2^{k+1} = \text{RHS}_4^k, \tag{33}$$

where

$$\begin{aligned}\text{RHS}_4^k = {} & \lambda_1\rho_3(\nabla_y u^{k+1} + c_2^k) + \lambda_1\rho_4\nabla_x^\top(p_{21}^k - d_{21}^k) \\ & + \lambda_1\rho_4\nabla_y^\top(p_{22}^k - d_{22}^k).\end{aligned}$$

The systems (32) and (33) have a circulatory structure and hence can also be solved by the fast Fourier transform.

The solution of the subproblems (28)–(31) can easily be obtained and explicitly computed by using a generalized shrinkage formula, as done by Wang *et al.* (2007). By simply computing, we have

$$\begin{cases} p_{11}^{k+1} = \max\left(s_{k+1} - \frac{1}{\rho_4}, 0\right) \cdot \dfrac{\nabla_x v_1^{k+1} + d_{11}^k}{s_{k+1}}, \\ p_{12}^{k+1} = \max\left(s_{k+1} - \frac{1}{\rho_4}, 0\right) \cdot \dfrac{\nabla_y v_1^{k+1} + d_{12}^k}{s_{k+1}}, \\ p_{21}^{k+1} = \max\left(s_{k+1} - \frac{1}{\rho_4}, 0\right) \cdot \dfrac{\nabla_x v_2^{k+1} + d_{21}^k}{s_{k+1}}, \\ p_{22}^{k+1} = \max\left(s_{k+1} - \frac{1}{\rho_4}, 0\right) \cdot \dfrac{\nabla_y v_2^{k+1} + d_{22}^k}{s_{k+1}}, \end{cases} \tag{34}$$

where

$$\begin{aligned} s_{k+1} = \Big(& (\nabla_x v_1^{k+1} + d_{11}^k)^2 + (\nabla_y v_1^{k+1} + d_{12}^k)^2 \\ & + (\nabla_x v_2^{k+1} + d_{21}^k)^2 + (\nabla_y v_2^{k+1} + d_{22}^k)^2 \Big)^{\frac{1}{2}}. \end{aligned} \tag{35}$$

The above shrinkage only requires a few operations so that the computation of per component in p^{k+1} is relatively fast.

2.5. ADMM algorithm. Combining the analysis in the above subsections, the ADMM type algorithm for the MR image reconstruction coupling model (7) is summarized in Algorithm 1.

3. Numerical implementation

In this section, some numerical implementations of the proposed model and algorithm will be given. All algorithms were implemented in MATLAB, v. R2017a. The experiments were performed on a personal computer with an i7 2.4 GHz processor, 16 GB memory and a Windows operating system. The first numerical comparison is between the proposed algorithm ADMM-TV^{2}L$_1$C and two existing algorithms by using the same images, including a four-year-old female pons MR image and a nine-year-old male's right vestibulo MR image. The numerical results illustrate that the proposed algorithm can reconstruct MR images more

Algorithm 1. ADMM-TV^{2}L$_1$C.

Require: $f, \rho_1, \rho_2, \rho_3, \rho_4, \gamma, \lambda, \lambda_1, \alpha, \beta, T$.

Initialize: $u^0 := \mathcal{F}^{-1}f, \delta_0 := 1, a_1^0 := a_2^0 := b^0 := c_1^0 := c_2^0 := 0; d_{11}^0 := d_{12}^0 := d_{21}^0 := d_{22}^0 := 0; p_{11}^0 := p_{12}^0 := p_{21}^0 := p_{22}^0 := 0, \kappa_1 := \kappa_2 := \kappa_3 := \kappa_4 := 1;$

for $k := 0 \to T-1$ **do**

Compute u^{k+1} by

$u^{k+1} := \mathcal{F}^{-1}(\hat{L}_1^k)^{-1}\mathcal{F}\text{RHS}_1^k,$

where $\hat{L}_1^k := \lambda\rho_2 I + \beta\delta_k I - \lambda_1\rho_3\mathcal{F}\Delta\mathcal{F}^\top,$

$\text{RHS}_1^k := \lambda_1\rho_3\nabla_x^\top(v_1^k - c_1^k) + \lambda_1\rho_3\nabla_y^\top(v_2^k - c_2^k) + \lambda\rho_2\Phi(z^k - b^k) + \beta\delta_k u^k - \beta A^\top(Au^k - f).$

if MSE $\le$ tol holds, **then**

Stop, and Go to 15:

end if

Compute θ^{k+1} by

$\theta^{k+1} := \mathcal{F}^{-1}(\hat{L}_2^k)^{-1}\mathcal{F}\text{RHS}_2^k,$

where $\hat{L}_2^k := \alpha I - \rho_1\mathcal{F}\Delta\mathcal{F}^\top,$

$\text{RHS} := \gamma\left((-\sin\theta^k, \cos\theta^k)\cdot \boldsymbol{v}^k\right),$

$\text{RHS}_2^k := \text{RHS}\left(|\boldsymbol{v}^k| - (\cos\theta^k, \sin\theta^k)\cdot\boldsymbol{v}^k\right) + \alpha\theta^k + \rho_1\nabla_x^\top(\eta_1^k - a_1^k) + \rho_1\nabla_y^\top(\eta_2^k - a_2^k).$

Compute $\eta_1^{k+1}, \eta_2^{k+1}, z^{k+1}$ by

$\eta_1^{k+1} := \max\left(t_{k+1} - \frac{1}{\rho_1}, 0\right)\cdot\dfrac{\nabla_x\theta^{k+1} + a_1^k}{t_{k+1}},$

$\eta_2^{k+1} := \max\left(t_{k+1} - \frac{1}{\rho_1}, 0\right)\cdot\dfrac{\nabla_y\theta^{k+1} + a_2^k}{t_{k+1}},$

$z^{k+1} := \text{shrink}(\Phi^\top u^{k+1} + b^k, \dfrac{g^{k+1}}{\rho_2}),$

where

$g_{k+1} := \left(1 - (\cos\theta^{k+1}, \sin\theta^{k+1})\cdot\frac{\nabla u^{k+1}}{|\nabla u^{k+1}|}\right)^2,$

$t_{k+1} := \sqrt{(\nabla_x\theta^{k+1} + a_1^k)^2 + (\nabla_y\theta^{k+1} + a_2^k)^2}.$

Compute v_1^{k+1}, v_2^{k+1} by

$v_1^{k+1} := \mathcal{F}^{-1}(\hat{L}_3^k)^{-1}\mathcal{F}\text{RHS}_3^k,$

$v_2^{k+1} := \mathcal{F}^{-1}(\hat{L}_3^k)^{-1}\mathcal{F}\text{RHS}_4^k,$

where $\hat{L}_3^k := \lambda_1\rho_3 I + \gamma g_{k+1} I - \lambda_1\rho_4\mathcal{F}\Delta\mathcal{F}^\top,$

$\text{RHS}_3^k := \lambda_1\rho_3(\nabla_x u^{k+1} + c_1^k) + \lambda_1\rho_4\nabla_x^\top(p_{11}^k - d_{11}^k) + \lambda_1\rho_4\nabla_y^\top(p_{12}^k - d_{12}^k),$

$\text{RHS}_4^k := \lambda_1\rho_3(\nabla_y u^{k+1} + c_2^k) + \lambda_1\rho_4\nabla_x^\top(p_{21}^k - d_{21}^k) + \lambda_1\rho_4\nabla_y^\top(p_{22}^k - d_{22}^k).$

Update $p_{11}^{k+1}, p_{12}^{k+1}, p_{21}^{k+1}, p_{22}^{k+1}$ via (34) and (35).

Update $a_1^{k+1}, a_2^{k+1}, b^{k+1}, c_1^{k+1}, c_2^{k+1}$ via (10).

Update $d_{11}^{k+1}, d_{12}^{k+1}, d_{21}^{k+1}, d_{22}^{k+1}$ via (25).

Update δ_{k+1} by

$\delta_{k+1} := \frac{\|A(u^{k+1} - u^k)\|_2^2}{\|u^{k+1} - u^k\|_2^2}.$

end for

return u^{k+1}.

effectively than the other two algorithms. Another comparison is between different sampling rates by using a nine-year-old male's right vestibulo MR image: the test results demonstrated that the proposed algorithm can yield higher quality image with a low staircase effect.

The quality evaluation of image reconstruction can be divided into subjective and objective. Subjective evaluation refers to the subjective qualitative evaluation of image quality, where the observer evaluates the details of the reconstructed image according to his own knowledge and understanding. Objective evaluation is an objective and qualitative evaluation of image quality based on scoring criteria, such as signal-to-noise ratio (SNR). In this paper, we use some real images as original ones to evaluate the quality of image reconstruction. In the following experiments, we define SNR based on traditional image reconstructive evaluation criteria as

$$\text{SNR}_1 = 10\log_{10}\left(\frac{\|u_{\text{true}}\|_2^2}{\|u - u_{\text{true}}\|_2^2}\right).$$

and mean squared error (MSE) as

$$\text{MSE} = \frac{1}{M \times N}\|u^{k+1} - u^k\|_2^2,$$

where u and u_{true} present the restored image and clean image, respectively, and $M \times N$ is the size of an image.

We select a centrally positioned region-of-interest (ROI) including 75% of the image, and define SNR based on MR image reconstructive evaluation criteria as

$$\text{SNR}_2 = \sqrt{2}\frac{S}{N},$$

where S is the mean pixel value of the ROI area in u_{true} and N is the standard deviation of noise of the ROI area (Och *et al*., 1992; Price *et al*., 1990).

Partially scanned data are obtained by non-uniformly randomly selecting some of the k-space samples from the entire k-space data of the tested MR images. For all the numerical experiments, we choose $\rho_1 = 10^{-3}$, $\rho_2 = 5 \times 10^{-3}$, $\rho_3 = 5 \times 10^{-3}$, $\rho_4 = 10^{-3}$, $\gamma = 10^{-3}$, $\lambda = 10^{-3}$ and $\lambda_1 = 2 \times 10^{-3}$. The parameters α, β connected with the sparsity of the underlying image and the noise level are fixed as $\alpha = 10^{-3}$, and $\beta = 0.9$, the termination criterion is fixed as $\text{MSE} = 5 \times 10^{-4}$.

3.1. Comparisons with other reconstruction algorithms. The main goal of this subsection is to compare the reconstruction effectiveness of three algorithms: the split Bregman algorithm for solving the TVL_1 model (2) (called SBA-TVL_1), the alternating direction method of multipliers for solving the TV^2L_1 model (3) proposed by Xie *et al*. (2014) (called ADMM-TV^2L_1), and the algorithm ADMM-$\text{TV}^2\text{L}_1\text{C}$ proposed in this paper. In the first experiment, we choose a four-year-old female pons MR image as the original image, which is accompanied by cavernous malformation and left abducens nerve palsy. The MR image is resized to 256×256. In order to test the performance of the proposed algorithm, the image is corrupted with Gaussian white noise at level $\sigma = 10$, and then the test data are obtained from the simulation of incomplete Fourier data with various sampling rates.

We show the reconstructed MR images in Fig. 1, which are obtained by the ADMM-$\text{TV}^2\text{L}_1\text{C}$, SBA-$\text{TVL}_1$, ADMM-$\text{TV}^2\text{L}_1$ algorithms with 36% k-space data for the four-year-old child's pons MR image. For better visual comparison, in the second row of Fig. 1, we zoom in on the central area to observe the texture features of these reconstructed images. We list SNR_1 and SNR_2 for the experimental results of the child's pons MR image under different k-space sampling rates from 28% to 46% in Tables 1 and 2, which show that our algorithm has better efficiency than the other two reconstruction algorithms.

The second experiment uses a nine-year-old male's right vestibulo MR image of size 198×198, with cochlear nerve hypoplasia and stenosis of the internal auditory canal. The SNR levels SNR_1 and SNR_2 are applied to compare the three algorithms with different sampling rates. The test data are obtained from simulation of different k-space sampling rates from 28% to 46% with a nine-year-old male's right vestibulo MR image. The SNR_1 and SNR_2 of the reconstructed MR images are given in Tables 3 and 4, respectively. These SNR data demonstrate that the SNR of the reconstructed images is improved as the sampling rate increases.

The reconstructed images with 36% k-space data and their zoomed-in images on central areas are shown in Fig. 2, where we can see that the images by reconstructed ADMM-$\text{TV}^2\text{L}_1\text{C}$ have better quality under the same sampling rate, and ADMM-$\text{TV}^2\text{L}_1\text{C}$ is more capable of recovering the textures and alleviating the staircase effect than SBA-TVL_1 and ADMM-TV^2L_1.

The third experiment also uses the four-year-old child pons MR image of size 198×198 to test the speed of three algorithms under a 28% to 46% k-space sampling rate. We use the mean squared error (MSE) of 5×10^{-4} as the stopping criterion for the iteration. The CPU times for three algorithms are shown in Table 5. The results demonstrate that the proposed algorithm is efficient and faster than SBA-TVL_1 and ADMM-TV^2L_1.

3.2. Comparisons under different sampling rates. In this subsection, in order to illustrate the proposed algorithm's performance, we make a comparison under different sampling rates from 26% to 44%. The test data are obtained from the simulation of human spinal joints MR images. The reconstructed images with different sampling rates are demonstrated in Fig. 3.

The first row images in Fig. 3 demonstrate four reconstructed human spinal joints MR images under

Table 1. SNR_1 via different algorithms and sample rates for the child pons image.

Sample rate	28%	30%	32%	34%	36%
SBA-TVL_1	19.14	19.61	19.71	19.84	19.97
ADMM-TV^2L_1	22.01	24.06	24.26	25.26	25.42
ADMM-TV^2L_1C	24.34	25.27	26.97	28.28	28.72
Sample rate	38%	40%	42%	44%	46%
SBA-TVL_1	20.50	20.35	21.09	21.43	21.66
ADMM-TV^2L_1	26.95	27.30	28.08	28.52	29.42
ADMM-TV^2L_1C	29.79	30.08	30.92	31.22	31.96

Table 2. SNR_2 via different algorithms and sample rates for the child pons image.

Sampling rate	28%	30%	32%	34%	36%
SBA-TVL_1	7.09	7.15	7.54	7.63	7.52
ADMM-TV^2L_1	10.60	11.36	11.58	11.88	12.06
ADMM-TV^2L_1C	11.71	12.16	12.50	12.72	12.93
Sampling rate	38%	40%	42%	44%	46%
SBA-TVL_1	8.10	7.90	8.24	8.15	8.44
ADMM-TV^2L_1	12.81	13.02	13.38	13.66	13.93
ADMM-TV^2L_1C	13.38	13.59	13.93	14.01	14.47

Table 3. SNR_1 via different algorithms and sample rates for child right vestibulo image.

Sampling rate	28%	30%	32%	34%	36%
SBA-TVL_1	24.61	24.85	25.05	25.54	25.41
ADMM-TV^2L_1	27.55	28.06	28.53	28.84	29.10
ADMM-TV^2L_1C	31.70	32.19	32.76	33.52	33.78
Sampling rate	38%	40%	42%	44%	46%
SBA-TVL_1	25.97	26.00	26.37	26.68	26.78
ADMM-TV^2L_1	29.49	29.52	29.71	30.02	30.37
ADMM-TV^2L_1C	34.30	34.56	35.23	35.36	35.71

Table 4. SNR_2 via different algorithms and sample rates for the child right vestibulo image.

Sampling rate	28%	30%	32%	34%	36%
SBA-TVL_1	7.64	7.96	7.82	8.11	8.03
ADMM-TV^2L_1	10.01	10.51	10.72	11.04	11.05
ADMM-TV^2L_1C	10.97	11.73	11.91	12.07	12.27
Sampling rate	38%	40%	42%	44%	46%
SBA-TVL_1	8.36	8.49	8.69	8.89	9.07
ADMM-TV^2L_1	11.92	12.15	12.42	12.77	13.09
ADMM-TV^2L_1C	12.51	12.85	12.94	13.30	13.50

Table 5. CPU times via different algorithms and sample rates for the child pons MR image.

Sampling rate	28%	30%	32%	34%	36%
SBA-TVL_1	2.45	2.40	2.27	2.27	2.30
ADMM-TV^2L_1	3.38	3.43	3.55	3.32	3.34
ADMM-TV^2L_1C	0.41	0.14	0.15	0.12	0.11
Sampling rate	38%	40%	42%	44%	46%
SBA-TVL_1	2.12	2.23	2.17	2.16	2.02
ADMM-TV^2L_1	3.11	1.86	1.38	1.30	1.18
ADMM-TV^2L_1C	0.10	0.09	0.09	0.09	0.09

different sampling rates from 26% to 44%, and the second row images correspond with zoomed-in details in the central area of the above four reconstructed images. The experimental results show that the proposed algorithm is stable and has a low staircase effect under different sampling rates.

4. Conclusion

Based on the deformations of the LOT model and second-order TV regularization, in this paper, we proposed an MR image reconstruction coupling model. In order to implement the proposed model, we applied the split Bregman iterative scheme twice, and by means of generalized shrinkage formulas, the shrink operator, and the diagonalization technique of the Fourier transform, we proposed an ADMM type algorithm. By making numerical experiments, we verified the feasibility and effectiveness of the proposed model and algorithm in two aspects.

First, in Section 2.1, we compared our proposed algorithm with the SBA-TVL_1 and ADMM-TV^2L_1 algorithms under different k-space sampling rates, from 28% to 46%. The numerical results indicated that the proposed algorithm can reconstruct MR images effectively. We listed the reconstructed MR images with a 36% sampling rate in Figs. 1 and 2, which demonstrated that the proposed algorithm can preserve diverse textures better than the other two algorithms. Then, in Section 2.2, we compared the proposed algorithm's performance under different sampling rates, from 26% to 44%, and listed the reconstructed images in Fig. 3, which showed that the proposed algorithm had stable performance with a low staircase effect under different sampling rates. However, we did not provide the convergence analysis of the proposed algorithm. It is going to be a topic for future research.

Acknowledgment

The research has been supported by the Natural Science Foundation of the Hunan Province of China (no. 2019JJ40323).

References

Chan, R.H., Yang, J. and Yuan, X. (2011). Alternating direction method for image inpainting in wavelet domains, *SIAM Journal on Imaging Sciences* **4**(4): 807–826.

Chen, Y., Hager, W., Huang, F., Phan, D. and Ye, X. (2012). A fast algorithm for image reconstruction with application to partially parallel MR imaging, *SIAM Journal on Imaging Sciences* **5**(1): 90–118.

Dong, F., Liu, Z., Kong, D. and Liu, K. (2009). An improved lot model for image restoration, *Journal of Mathematical Imaging and Vision* **34**(1): 89–97.

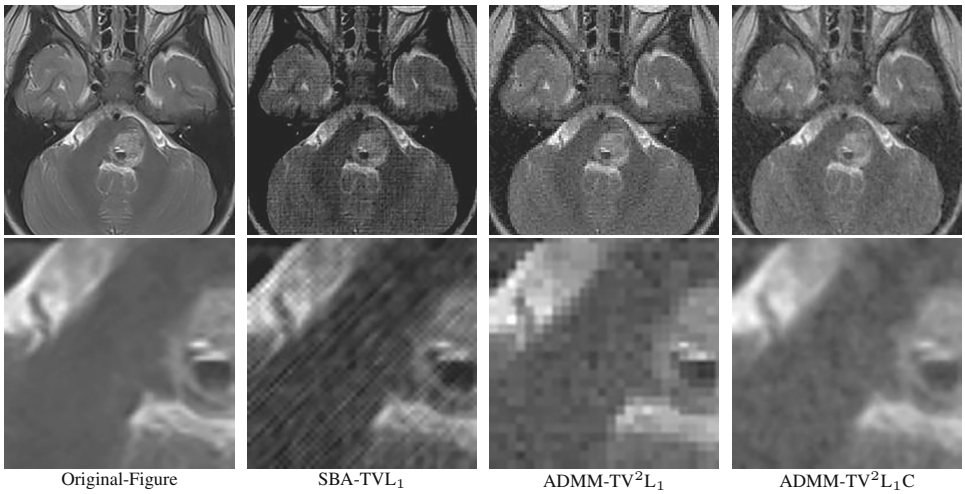

Fig. 1. Child pons MR image reconstruction via different algorithms with a 36% sample rate.

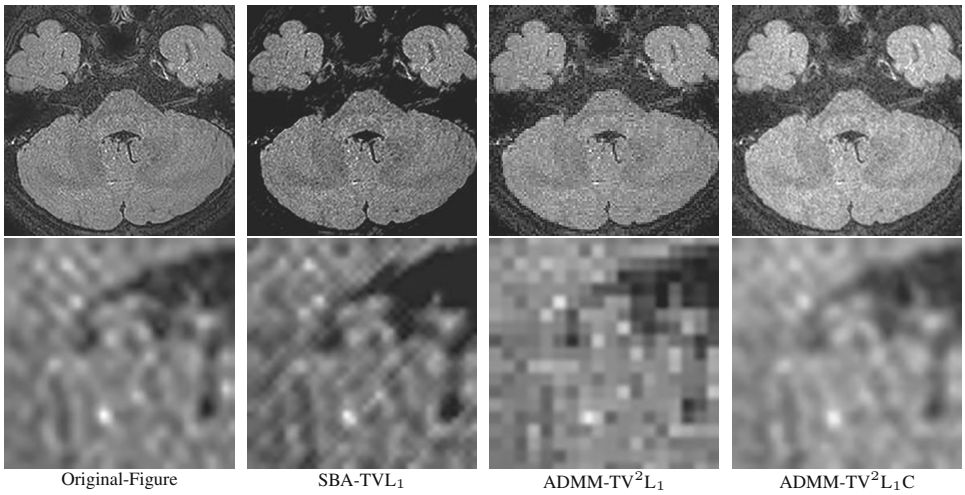

Fig. 2. Child right vestibulo MR image reconstruction via different algorithms with a 36% sample rate.

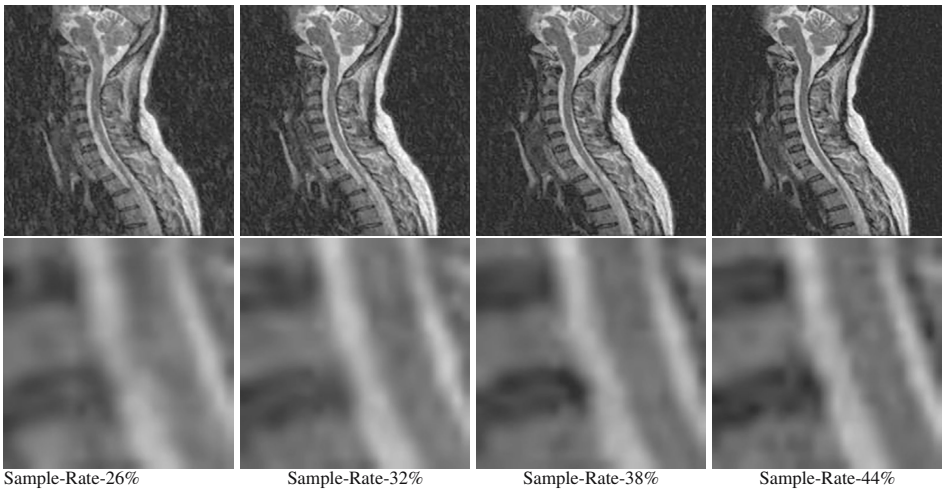

Fig. 3. ADMM-TV^{2}L$_1$C reconstruction for the human spinal joints MR image with a 26% to 44% sampling rate.

Hao, Y., Feng, X.C. and Xu, J.L. (2012). Split Bregman algorithm for a novel denoising model, *Journal of Electronics and Information Technology* **34**(3): 557–563.

Lustig, M., Donoho, D. and Pauly, J.M. (2007). Sparse MRI: The application of compressed sensing for rapid MR imaging, *Magnetic Resonance in Medicine* **58**(6): 1182–1195.

Lysaker, M., Lundervold, A. and Tai, X.C. (2003). Noise removal using fourth-order partial differential equation with applications to medical magnetic resonance images in space and time, *IEEE Transactions on Image Processing* **12**(12): 1579–1590.

Lysaker, M., Osher, S. and Tai, X.C. (2004). Noise removal using smoothed normals and surface fitting, *IEEE Transactions on Image Processing* **13**(10): 1345–1357.

Miao, J., Wong, W.C.K., Narayan, S., Huo, D. and Wilson, D.L. (2011). Modeling non-stationarity of kernel weights for k-space reconstruction in partially parallel imaging, *Medical Physics* **38**(8): 4760–4773.

Och, J., Clarke, G. and Sobol, W.T. (1992). Acceptance testing of magnetic resonance imaging systems: Report of AAPM nuclear magnetic resonance task group no. 6, *Medical Physics* **19**(1): 217–229.

Price, R.R., Axel, L., Morgan, T., Newman, R., Perman, W., Schneiders, N., Selikson, M., Wood, M. and Thomas, S.R. (1990). Quality assurance methods and phantoms for magnetic resonance imaging: Report of the AAPM nuclear magnetic resonance task group no. 1, *Medical Physics* **17**(2): 287–295.

Rudin, L.I., Osher, S. and Fatemi, E. (1992). Nonlinear total variation based noise removal algorithms, *Physica D: Nonlinear Phenomena* **60**(1–4): 259–268.

Steidl, G. (2006). A note on the dual treatment of higher order regularization functionals, *Computing* **76**(1–2): 135–148.

Wang, Y., Yin, W. and Zhang, Y. (2007). A fast algorithm for image deblurring with total variation regularization, *CAAM technical report,* Rice University, Houston, TX, pp. TR07–10.

Wright, S.J., Nowak, R.D. and Figueiredo, M.A.T. (2009). Sparse reconstruction by separable approximation, *IEEE Transactions on Signal Processing* **57**(7): 2479–2493.

Xie, W.S., Yang, Y.F. and Zhou, B. (2014). An ADMM algorithm for second-order TV-based MR image reconstruction, *Numerical Algorithms* **67**(4): 827–843.

Yang, J., Zhang, Y. and Yin, W. (2010). A fast alternating direction method for TVL1-L2 signal reconstruction from partial Fourier data, *IEEE Journal of Selected Topics in Signal Processing* **4**(2): 288–297.

Yang, Y.F., Pang, Z.F., Shi, B.L. and Wang, Z.G. (2011). Split Bregman method for the modified lot model in image denoising, *Applied Mathematics and Computation* **217**(12): 5392–5403.

Ye, X., Chen, Y. and Huang, F. (2011). Computational acceleration for MR image reconstruction in partially parallel imaging, *IEEE Transactions on Medical Imaging* **30**(5): 1055–1063.

You, Y.L. and Kaveh, M. (2000). Fourth-order partial differential equations for noise removal, *IEEE Transactions on Image Processing* **9**(10): 1723–1730.

Bo Zhou received his MSc degree computer application at the Computer Department of Hunan University. He is a PhD candidate in the College of Mathematics, Hunan University. His main research interests include digital image processing, artificial intelligence, and electronic chip design.

Yu-Fei Yang is a professor and a PhD supervisor in the College of Computer Engineering and Applied Mathematics, Changsha University, and the School of Mathematics, Hnman University. His main research interests include digital image processing, numerical methods and applications in inverse problems of PDEs, optimization theory and methods.

Bo-Xia Hu received his MSc degree from the Hunan University School of Mathematics in 2006. He is a PhD candidate in the College of Mathematics, Hunan University. His present research interests include digital image processing, variational inequality, optimization theory and methods.

Received: 18 October 2018
Revised: 16 March 2019
Re-revised: 26 May 2019
Accepted: 8 July 2019